Coverage Induced Chiral Transition of Co(II)-5,15-Diphenylporphyrin Self-Assemblies on Cu(111)

Feifei Xiang†, M. Alexander Schneider**

Solid State Physics, Friedrich-Alexander-Universität Erlangen-Nürnberg (FAU), Staudtstr. 7, 91058 Erlangen, Germany

KEYWORDS: scanning tunneling microscopy, chiral recognition, chiral separation, porphyrin, van der Waals interaction

ABSTRACT

Wallach's rule elucidates the phenomenon that racemic crystals are denser than their enantiopure form. The rule applies to most chiral molecular systems with the exception of some amino acids. However, it remains unclear whether Wallach's rule applies to the special but important class of chiral systems where chirality is induced by the adsorption of prochiral molecules on substrates. In this work, we show that the exemplary system, Cobalt(II)-diphenylporphyrin (Co-DPP) on Cu (111), follows Wallach's rule. Co-DPP assumes chiral isomers upon adsorption and shows a phase transition from an enantiopure linear chain structure to a racemic close-packed structure with increasing molecular density. Density functional theory (DFT) reveals that the chiral recognition, separation and phase mixture of Co-DPP are due to the synergistic mechanism of substrate-molecule and molecule-molecule interactions.

INTRODUCTION

A chiral object cannot be superimposed over its mirror image by mere rotations. Chirality is ubiquitous in nature, and plays a vital role in determining the functionality of proteins in bio-systems[1–4], catalytic activities of enzymes[5] and effectivity of chiral drugs[6]. Enantiomer (chiral) recognition, separation and transfer on the one hand and enantioselective synthesis on the other, are key challenges in such chiral systems. Deeper insight into these phenomena allows one to optimize the asymmetric catalytic routes, improve the yield of desired enantiomer products and even gain more understandings of the origin of homochirality in living systems.

One way forward is to reduce the complexity of the problem and to focus onto two-dimensionally confined chiral systems[7], represented by *e.g.* molecules on a solid surface. Molecular symmetries may be broken upon adsorption, allowing prochiral species to assume chiral configurations or self-assemblies on the surface.[8–12] These provide prototypical testbeds for understanding the mechanism of chiral recognition, separation and transfer. One of the findings in chiral self-organizations is that the racemic crystals tend to have higher density than their homochiral crystals, which is misnamed as Wallach's rule[13]. It applies to a wide range of chiral organic systems[14–16]. However, many other exceptions reveal that in some conditions, for example, some organic salts[17], amino acids[18], and in low crystallization temperatures[19], the crystals prefer to have conglomerate packing, in which the crystals consist of homochiral regions. Upon adsorption on surfaces, the crystallization of molecules may be altered from their three-dimensional (3D) cases due to the reduction of molecular symmetry and the interactions with the substrates. It has recently been shown that chiral molecules, such as helicene[20], polyalanine[21], undergo chiral self-assembly transition from homochiral to racemic structures as a function of coverage on achiral substrates. Meanwhile, various factors, such as concentrations[22], temperature[23],

charge transfer[24,25], interactions between molecules, *e.g.* hydrogen bonding[26–28], van der Waals interactions[29,30], and dipole interactions[21], were identified to influence the chiral self-organization, sometimes in a delicate and cooperative interplay[20]. Therefore, it is important to investigate the mechanisms behind homochiral and racemic packing on surfaces, where the subtle interplay between molecule-substrate and molecule-molecule interaction is interwoven with the expression of chirality of prochiral adsorbates.

Porphyrins are one of essential building blocks in living systems for photosynthesis and oxygen transport. Their specific electronic and magnetic properties have given rise to significant applications in various electronic devices[31–36]. A porphyrin ideally has D_4 symmetry; however, due to the intrinsic flexibility of the porphyrin macrocycle, the conformation of a porphyrin can be highly tuned by the interaction with substrates[12,37,38], substitution at porphyrin backbones[39,40], and metalation[41], which all modify the adsorption behavior and the physical and chemical properties of porphyrins.

In order to gain more insight into the formation of chiral configurations on the surface, chiral transfer in self-assembly structures, and the phase transition between enantiopure to racemic structures, here in this work, we chose cobalt metalated diphenlyporphyrin (Co(II)-5,15-diphenylporphyrin, Co-DPP) as a test molecule and studied its adsorption behavior and chiral self-assemblies on the Cu(111) surface using scanning tunneling microscopy (STM). Single Co-DPP adopts a chiral configuration due to the interaction with substrate. As a function of coverage, the self-assembly of Co-DPP undergoes a structural phase transition from an enantiopure chiral chain self-assembly to a racemic close-packed (RCP) structure. Density functional theory (DFT) suggests that the chiral phase transition of Co-DPP is due to a synergistic effect of molecule-molecule interaction and molecule-substrate interactions.

METHODS

STM

The experiments were carried out in a home-built scanning tunneling microscopy operated in ultra-high vacuum with a base pressure of ~4×10^{-11} mbar at 80K. A Cu (111) single crystal (Surface Preparation Lab) was cleaned by several cycles of Ne ion bombardment at 1×10^{-4} mbar, followed by annealing to 810 K for 5 mins. After that, Co(II)-5,15-diphenylporphyrin (Co-DPP, PorphyChem SAS, purity: 98%) was deposited on the clean Cu (111) surface kept at 300 K with a deposition rate of ~0.06 ML min^{-1} (1 ML refers to 0.7 molecules/nm^2). The samples were subsequently transferred to the STM chamber and cooled down to ~80K for STM measurements. All the STM images were acquired in constant current mode using an etched tungsten tip with the bias voltage applied to the sample. The STM images were subsequently analyzed with the help of the WSxM software[42].

Computational Details

DFT calculations were performed by the Vienna Ab-initio Simulation Package (VASP)[43,44], using the projector augmented wave method (PAW)[45] and the generalized gradient approximation (GGA)[46], and its implementation of the optB86b functional for treating vdW forces[47]. We used an energy cutoff of 400 eV STM simulations were performed by using the Tersoff–Hamann approximation.[48]

Several steps were performed to sample the adsorption potential landscape of the molecule. First, a 8×8 4-layer Cu(111) slab with the appropriate lattice parameter was constructed. The slab was relaxed structurally using a 2×2×1 Γ-centered k-point mesh and keeping the bottom two layers fixed. On this slab, the Co-DPP molecule was placed at the desired orientation and the position of the molecular atoms were relaxed to forces smaller than 0.05 eV/Å using the Γ-point only keeping

the lateral positions of the Co atom fixed. The size of the repeated surface cell ensured that at any orientation the atoms of neighboring molecules are more than 3.4 Å apart (coverage 0.24 molecule/nm^2). Finally, the coordinates of the molecule and the top two slab layers were relaxed using the same parameters. We observe that the energy gain when relaxing the substrate amounts to 100-200 meV.

Only the configuration of the Co-DPP in bridge position with minimal energy was further relaxed to forces below 0.01 eV/Å. This reduced the energy further by 15 meV and introduced changes in the atomic positions < 5 pm. This and the energy difference between symmetry related configurations on the threefold symmetric adsorption sites (hollow and top sites) give us confidence that the relative energies are correct to within 20 meV.

To calculate the geometry optimizations of chain and RCP structures, the residual force per atom was less than 0.02 eV/Å. Two molecules in the chain or RCP layout are each placed on a $7 \times 4\sqrt{3}$-rect and a $8 \times 4\sqrt{3}$-rect 4-layer Cu slab. This resulted in slightly different molecular model coverages of 0.63 and 0.55 molecules / nm^2, respectively. The Co-DPP configuration used in these two models is derived from the geometry optimized single Co-DPP that orientates the molecule at 16° with respect to the $[1\bar{1}0]$ direction of the substrate and on a bridge site.

The adsorption energy per Co-DPP, E_{ad} in the chain and RCP structure respectively is defined as

$$E_{ad} = (E_{mol+sub} - E_{sub})/2 - E_{mol}$$

where the $E_{mol+sub}$ is the total energy of the two Co-DPP on (7×4√3)-rect and (8×4√3)-rect Cu(111) supercells respectively. E_{mol} and E_{sub} are the energy of a fully relaxed Co-DPP in the gas phase and the corresponding Cu(111) slabs, respectively. Only Γ-point calculations were performed.

Tests with larger k-point sampling (*i.e.* 2×2×1) were done and the energy difference between configurations was found to be consistent.

For comparison, the total energy as a function of molecule-molecule distance in the chain and RCP structures was calculated in the gas phase. The Co-DPP starting configuration used in these calculations was taken as the geometry optimized single Co-DPP on Cu(111) on a bridge site. All the molecular atoms in the molecule were kept fixed, therefore, the energy change with respect to molecule-molecule distance is mainly driven by vdW forces.

RESULTS AND DISCUSSION

Different amounts of Co-DPP was deposited on a clean Cu (111) kept at room temperature using the same deposition rate (see Methods). STM images of the coverage dependent self-assembly structures of Co-DPP are shown in Fig.1 (a)-(d). High-resolution STM images show that Co-DPP has two mirror symmetric configurations on the surface, named L-Co-DPP and R-Co-DPP respectively (Fig. 1(e)-(h)). Here, we classify the self-assembly structures at the surface as "enantiopure" if molecules form structures in which molecules of different chirality are well separated from each other and hence have only negligible interaction with each other. Conversely, a structure is classified as "racemic" if molecular interactions between the two chiral molecular configurations are found. Below half a monolayer (~0.34 molecules / nm^2), Co-DPP forms ring and linear chain structures (Fig. 1(a), (b), (e), (f)). The ring structure only appears at very low coverages, already at 0.16 molecules / nm^2 only chains are observed. The appearance of the ring structure and the competing growth mechanism between the ring and linear chain structures could be due to the high-dilution principle[49,50]. In our experiments, such conditions are met only at an extremely low coverage (0.04 molecules / nm^2 in Fig.1(a)) due to the relatively high deposition rate. High-resolution STM images indicate that ring and linear chain structures are formed by

enantiopure Co-DPP molecules (Fig. 1(e) and (f)), hence the ring and linear chain structures also show chirality. It is worth noting that the ring and linear chain structures of different chirality are well separated at low molecular coverage. However, as soon as the density of Co-DPP is > 0.34 molecules / nm^2 (half monolayer coverage), the linear chains with different chirality start to intermix with each other and form two-dimensional crisscross-like networks (Fig. 1(c) and (g)). At the crossing points, L- and R-Co-DPP molecules alternatively pack with each other, forming a racemic close-packed (RCP) structure (Fig. 1(g)). Further increasing the surface density to 0.7 molecules / nm^2 (full monolayer coverage), Co-DPP forms densely packed structures, in which the chirality of Co-DPP cannot be distinguished anymore (Fig.1 (d) and (h)). Several reasons are considered leading to the failure of the identification of chirality of Co-DPP in the dense phase: The saddle shape configuration of Co-DPP might be transferred to less distorted configuration due to the reduction of molecule-substrate interactions[51], resulting in an achiral appearance in STM. Alternatively, the Co-DPP may form enantiopure self-assembly structure in such high dense coverage. A formation of random mixture of the two chiral enantiomers may also lead to the disordered phase appearing achiral in STM.[52]

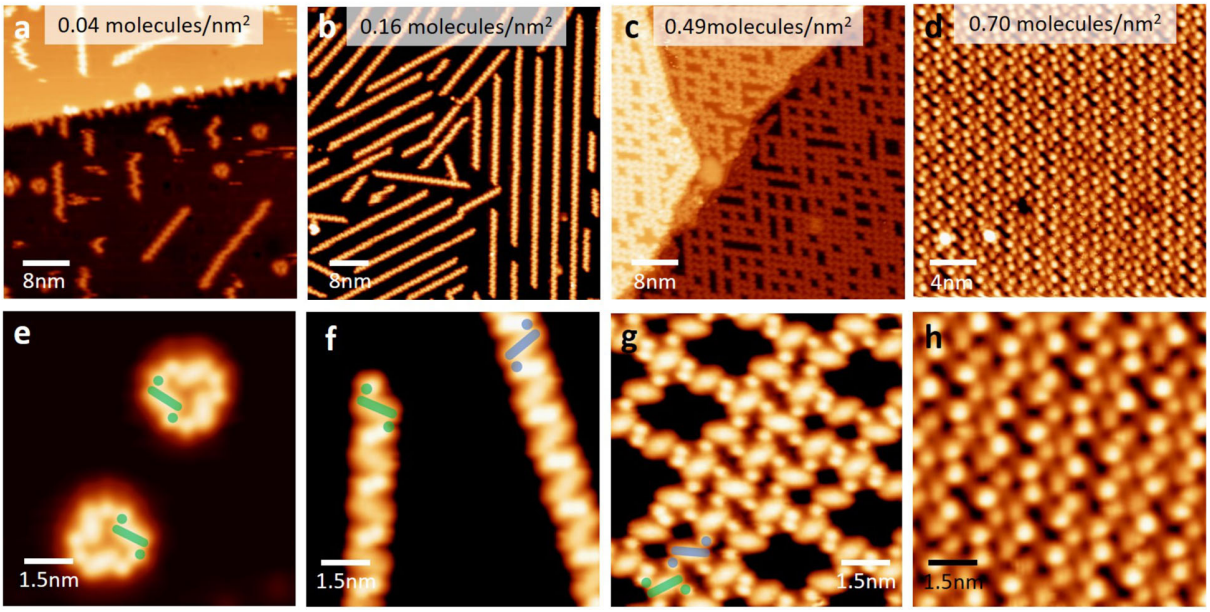

Figure 1 Large scale (a)-(d) and zoomed in (e)-(h) STM images of self-assembly structures of Co-DPP on Cu(111) at different molecular coverages. The corresponding coverage is shown in (a)-(d), it is defined as the average area density set by the preparation. The blue and green patterns overlaid in (e)-(g) indicate the two mirror symmetric Co-DPP configurations. (a) U = -2 V, I = 0.26 nA, (b) U = -1.7 V, I = 0.27 nA, (c) U = -1.15 V, I = 0.27 nA, (d) U = -1.74 V, I = 0.2 nA, (e) U = -1.8 V, I = 0.26 nA, (f) U = -1.7 V, I = 0.27 nA, (g) U = -1.15 V, I = 0.27 nA, (h) U = -1.74 V, I = 0.2 nA.

In order to understand the formation of chiral Co-DPP configurations we investigate in more detail their appearances in STM images and their structure from DFT calculations (Fig. 2). On the surface, isolated molecules are only found adsorbed at step edges and they appear also as L- and R-Co-DPP as shown in Fig. 2(a). The structural relaxation of Co-DPP on Cu(111) reveals that Co-DPP assumes a saddle-shape configuration, where the pyrrolic rings in the diagonal position in Co-DPP macrocycle are slightly tilted up (Fig. 2(b) and (c)). The corresponding STM image simulation explains the molecular appearance very well (Fig. 2(d)).

The saddle-shape configuration is caused by intramolecular (steric) interactions between the phenyl rings and the macrocycle. As a result, one of the pyrrolic rings adjacent to each phenyl ring slightly tilts up, while the other neighboring pyrrolic ring remains flat (Fig. 2(b), (c)). The tilted-up pyrrolic rings are diagonally opposite to each other and are imaged brighter than the other two flat pyrrolic rings in STM (Fig. 2(d)). This, in combination with the turning sense of the phenyl rings (a right-handed or left-handed screw), makes the molecule chiral on the surface. The chirality and the symmetry of the molecule on different adsorption sites is also reflected in the DFT total energy dependence on adsorption site and on angular orientation (Fig. 2(e)), where we define the position of the central Co ion as the adsorption site of the molecule. The adsorption energy of the less-favorable top and two hollow sites have a period of 60° with respect to the orientation of the molecular axis, due to the combination of C_2 and C_3 symmetry of molecule and substrate, respectively. Conversely, on the two-fold symmetric bridge site the same energy is only reached after 180° rotation. Furthermore, the three possible bridge-site configurations within the Cu (111) unit cell are degenerate only when occupied by molecules of different orientation or chirality (Fig. 2(e)). So a degenerate configuration of the L-molecule is found at 16°±60° orientation, which however entails a lateral shift of the molecule. Similarly, a degenerate configuration of the R-molecule is found by mirror operation (Fig. 2(f)). In all, we find the minimum energy of the system for bridge site adsorption at 10° with respect to the $[1\bar{1}0]$ direction. This agrees well with the experimental observation that L-Co-DPP shows an orientation of 16° with respect to $[1\bar{1}0]$.

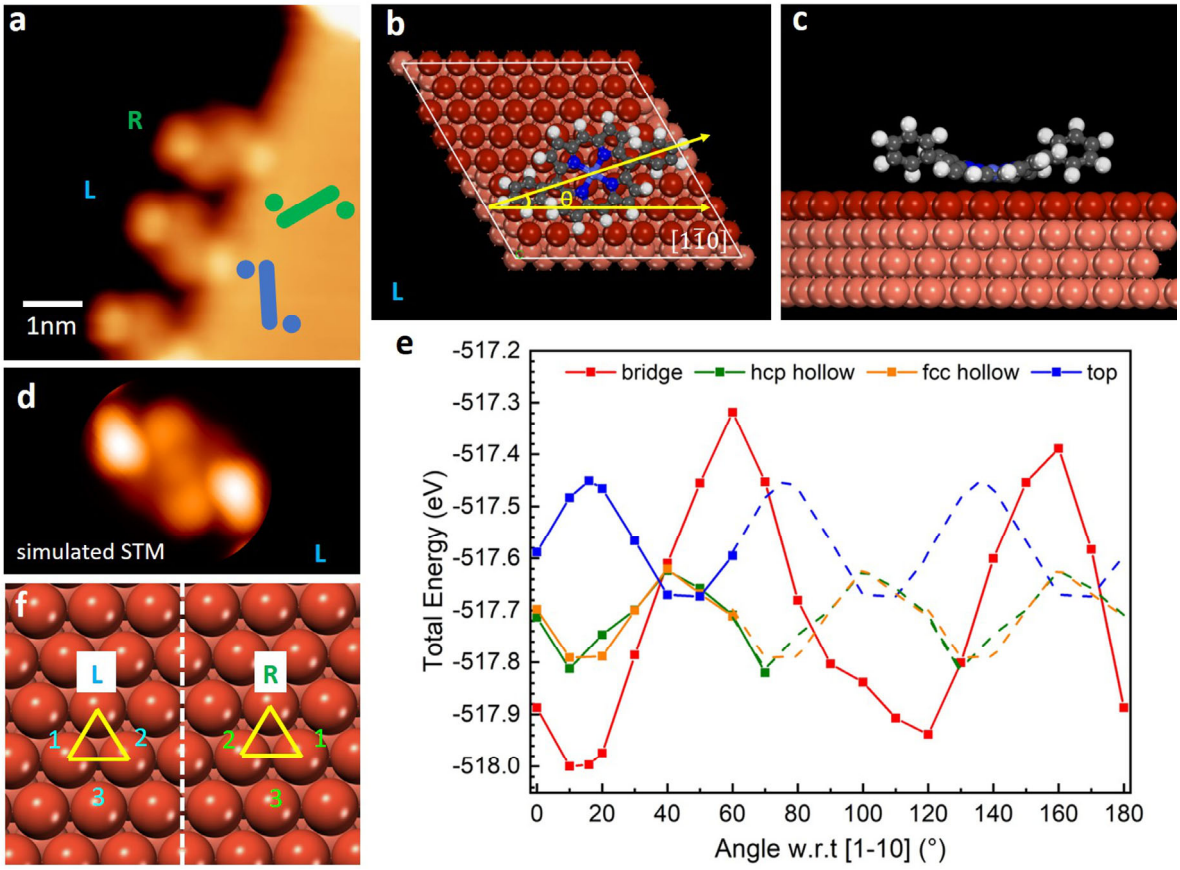

Figure 2 The configuration of Co-DPP with different chirality on Cu (111). (a) STM image of a L- and a R-Co-DPP attached on a step edge. U = -2.0 V, I = 0.3 nA. (b) Top view and (c) side view (looking through $[11\bar{2}]$) of geometric optimized chemical structure of L-Co-DPP on a Cu (111) slab. (d) Simulated STM image of L-Co-DPP from (b) with a bias voltage of -2 V. (e) The diagram of total energy of a L-Co-DPP at different adsorption sites at different rotational angles between the long axis of L-Co-DPP and $[1\bar{1}0]$ of the Cu (111) substrate. (f) The preferred adsorption sites of L- and R-Co-DPP. The adsorption sites and the corresponding adsorption energies are related by mirror symmetry of molecule and substrate.

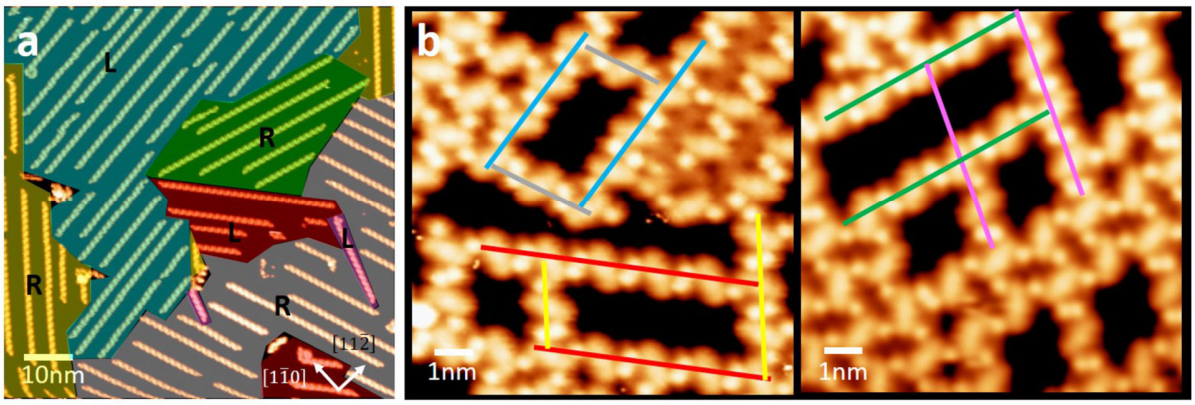

Figure 3 (a) Large scale STM image that contains chain structure domains with 6 different orientations. Each domain is marked by a different color mask. The chirality of Co-DPP in each domain is given in the image. U = -2.1 V, I = 0.27 nA. (b) STM images of crisscross networks with three different orientations. The orientation of the chain found in crisscross networks is the same as the orientation of the chain structures shown at low molecular coverages. U = -1.8 V, I = 0.26 nA, U = -1.15 V, I = 0.27 nA.

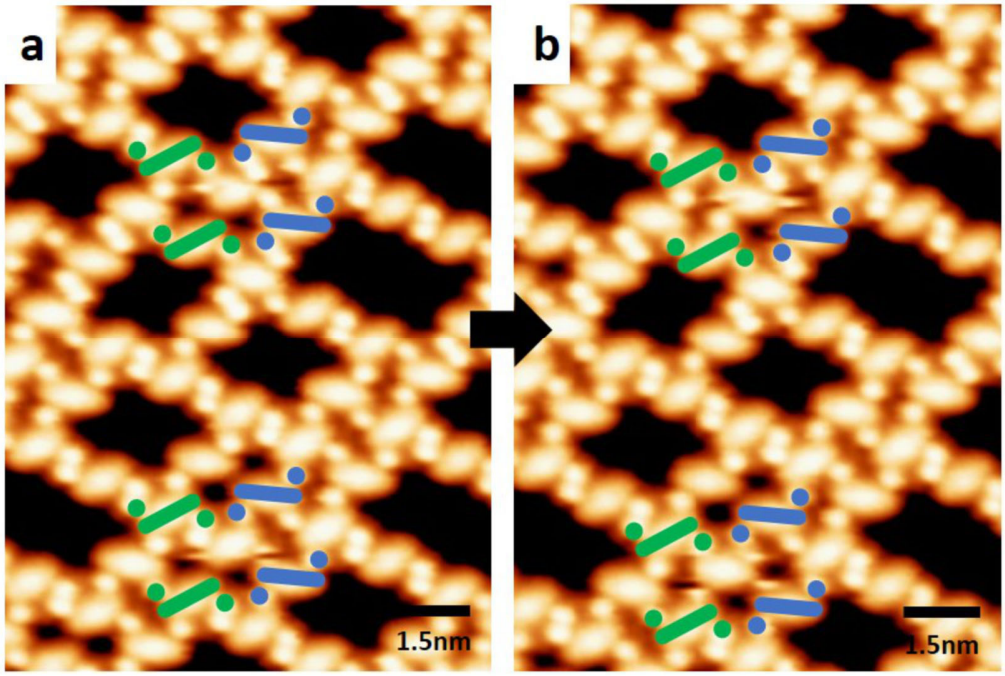

Figure 4 Chirality switch of Co-DPP in the network structure. Before (a) and after (b) the configuration change of Co-DPP molecule. (a) and (b) were taken consecutively. The chirality of the surrounding Co-DPP species are given in the figures.

Next, we will consider the phase transition from the enantiopure 1D chain structure to the 2D RCP structure as a function of molecular coverage. The orientation of the single molecule on the surface is maintained within the self-assembly chain structures. As a consequence, the L- and R-chains appear in three orientations on the surface. Similarly, oriented L- and R-chains enclose an angle of 20° with each other and therefore, quite generally, enantiopure domains may be packed closer than mixed domains. This is observed at low coverage (Fig. 3(a)). Also in the network structures, the original orientation of the L- and R-chains may still be identified (Fig. 3(b)). Two conceivable mechanisms are behind the formation of larger enantiopure domains on the one hand and racemic networks on the other. The first is diffusion of molecules and chiral control of structure nucleation by molecule-molecule interactions. This is the dominant process for low coverage. Molecules will diffuse and only nucleate with partner molecule of the correct chirality. In the present system, this is a molecule of the same chirality but in general may also be a partner of opposite chirality. If a molecule cannot change its chirality, then at larger coverage this mechanism must lead to racemic structures like the networks also found here consisting of short, enantiopure chain segments. A second mechanism may be the switching of chirality on the surface, which is conceivable for prochiral molecules like in the present case. While we do not observe switching of molecules when they are incorporated into chain or network structures, we observe it for single molecules trapped in pores of the molecular network even at 80 K as shown in Fig. 4.

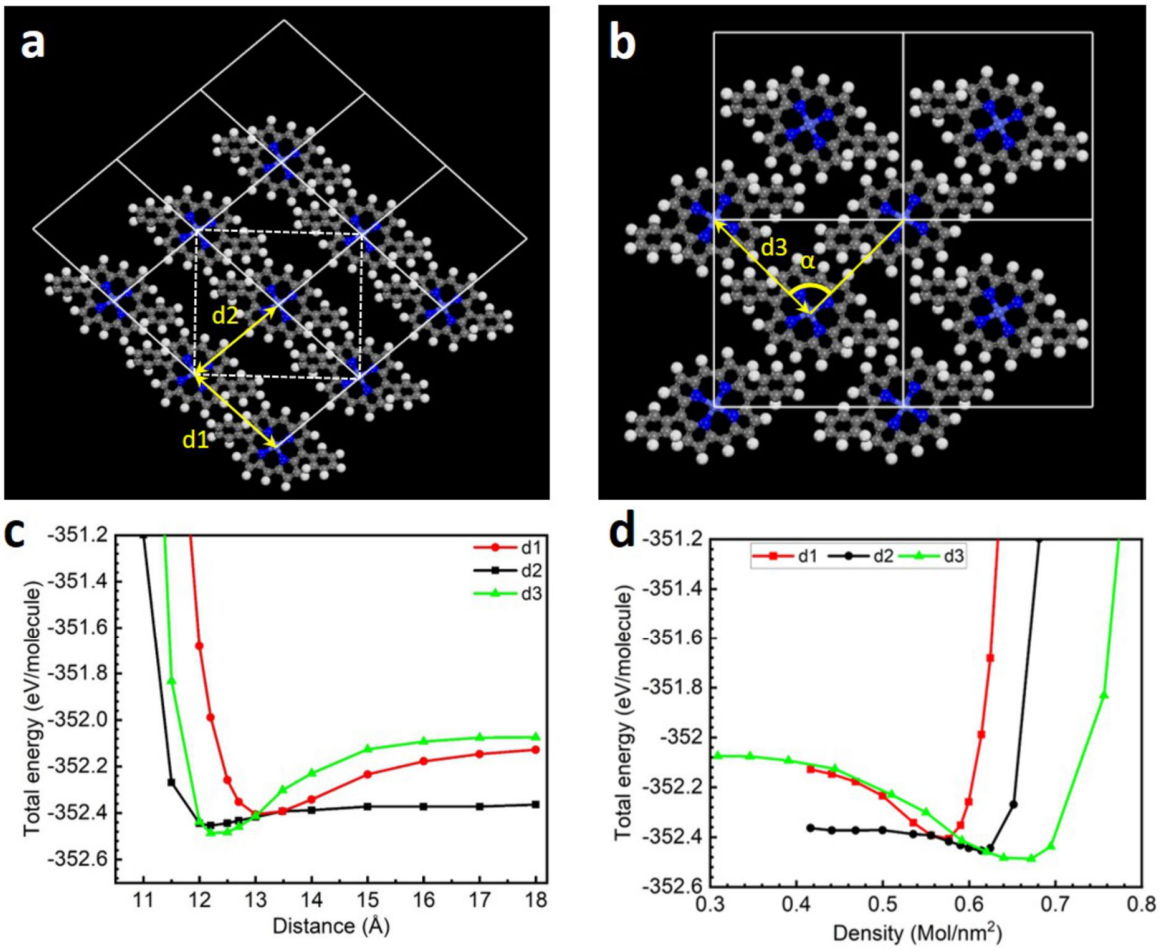

Figure 5 Gas phase model of (a) chain and (b) RCP unit cell. (a) d1 and d2 are defined as the molecule-molecule distance in a chain and between the chains, respectively. The size of the unit cell is determined by keeping d2 (or d1) at the optimal value while varying d1 (or d2). (b) The RCP structure is determined by d3 and angle α. d3 is defined as the distance between the two adjacent Co centers in L- and R-Co-DPP in the RCP structure, while the definition of α is shown in (b). α was fixed when varying d3 in order to varying the RCP unit cell size. (c) Diagram of the calculated total energy of a gas phase Co-DPP in the chain and RCP structure as a function of molecule-molecule distance. (d) Data of (c) as function of molecular areal density.

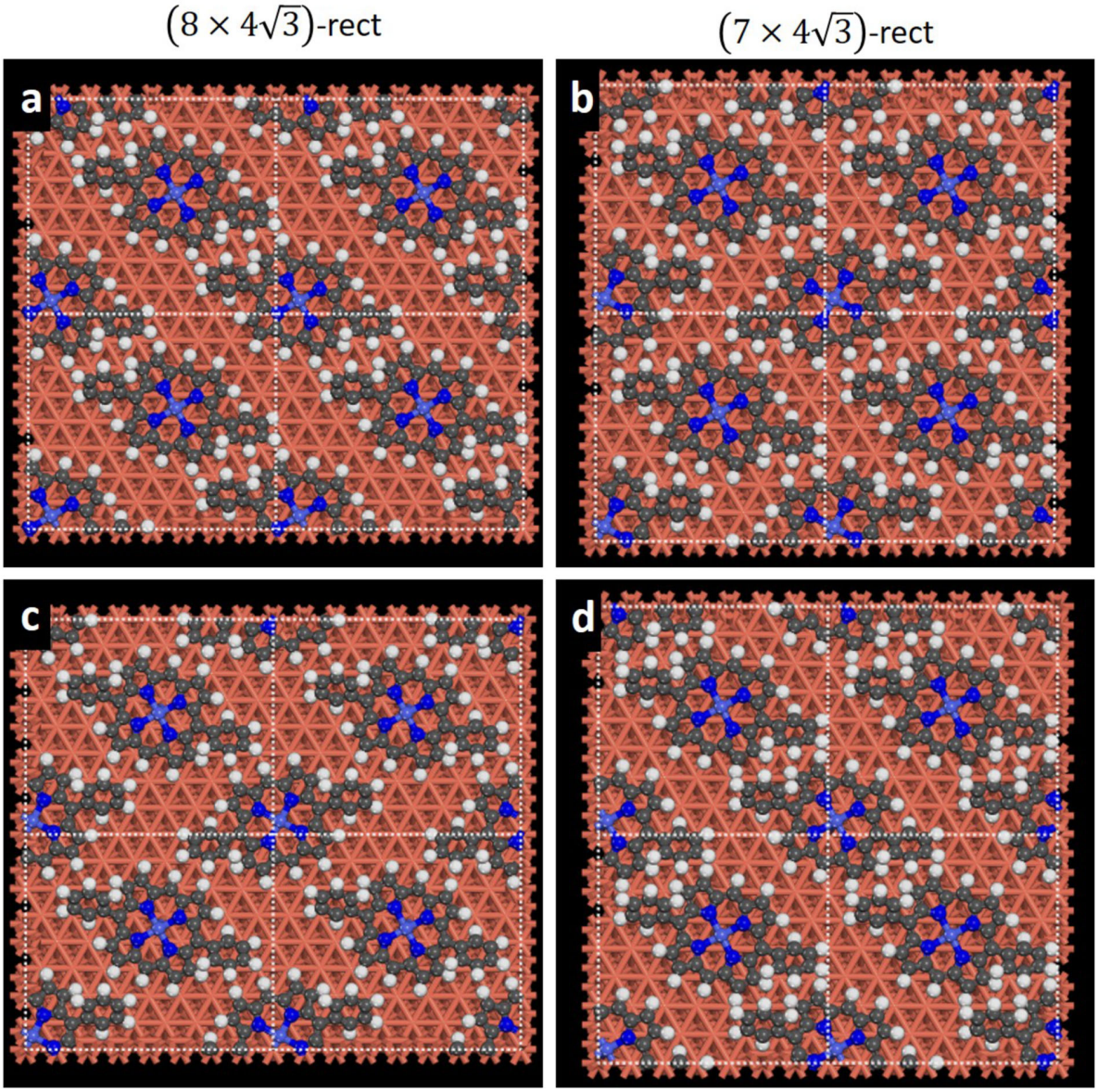

Figure *6* Lowest energy configuration for the linear chain and the RCP structural model on Cu (111) slabs. (a) Chain unit cell on a $(8 \times 4\sqrt{3})$-rect slab. (b) RCP structure unit cell on a $(7 \times 4\sqrt{3})$-rect slab. (c) RCP structure unit cell on a $(8 \times 4\sqrt{3})$-rect slab. This configuration has an adsorption energy E_{ad} that is 213 meV per molecule higher than the chain structure shown in (a). (d) Chain structure on a $(7 \times 4\sqrt{3})$-rect slab. This configuration has 175 meV per molecule

higher E_{ad} than the RCP structure shown in (b). The L- and R-Co-DPP in (a) and (b) adsorb at their preferred bridge sites.

If the molecules can switch their chiral state on the surface then, of course, the question arises why the system does not form large domains of closely packed enantiopure chains at high coverage. To this, we find an answer from DFT, highlighting the delicate balance of the interactions at play. First, we studied the molecule-molecule interaction in the linear chain and RCP structures by varying the molecule-molecule distance (d1 for varying intra-chain interaction, d2 for varying inter-chain interaction, and d3 for varying inter-molecular interactions in RCP structure) in the gas phase (Fig. 5(a), (b)). The interaction between the Co-DPP in the chain is as strong as 26.7 kJ / mol (Fig.5(c)), which we attribute to the π-π style interactions[53,54] between the phenyl rings and pyrrolic rings from two neighboring molecules. In contrast, the interaction between the chains is 8.68 kJ / mol, confirming that the linear chain is mainly stabilized by the intra-chain interaction. Conversely, in the RCP structure, a Co-DPP interacts with another four Co-DPP with the opposite chirality, resulting in an energy gain of 39.7 kJ / mol. By varying d1, d2 and d3 in the linear chain and RCP structure, we noticed that the π-π style interaction (intra-chain interaction) in the chain is more distance sensitive, while the van der Waal (vdW) interaction is more tolerant to molecule-molecule distance. On the other hand, the vdW interaction becomes comparable in energy to the π-π style interaction[55,56] only at short molecule-molecule distances where the latter starts to enter the repulsive regime.

In order to link the system total energy to molecular coverages, we converted the molecule-molecule distance into molecule density S defined as,

$S = N_{mol}/A$

where N_{mol} is the number of molecules in the unit cell, and A is the area of the unit cell defined by d1, d2 or d3 (Fig. 5(d)). Indeed, at a molecular coverage ≤ 0.62 molecules / nm^2, the linear chain structure is energetically more favorable than the RCP structure. It is worth noting that at the molecular density range 0.59-0.62 molecules / nm^2, the energy difference between linear chain and RCP structure is within 20 meV per molecule, indicating the possible coexistence of linear chain and RCP structures. In experiment, this is already observed at much lower density (Fig. 1(c)) and may be a consequence of the templating effect of the substrate that has not been considered up to here. To understand this, we performed the geometric optimization calculation of the linear chain and RCP structural models on a $\left(8 \times 4\sqrt{3}\right)$-rect and a $\left(7 \times 4\sqrt{3}\right)$-rect Cu slab respectively to make sure that L- and R-Co-DPP adsorb at their preferred bridge sites as shown in Fig. 2(f) and Fig. 6 (a), (b). In the linear chain structure, Co-DPP orientates at 16° with respect to [1 -1 0] (Fig. 6(a)) and remains in the same orientation as the single molecule. The linear chain model shown in Fig. 6(a) has a molecular density of 0.55 molecules / nm^2 with the chain-chain distance of 13.4 Å, which is still close enough for chain-chain interaction to further lower the system energy. At this molecular density the linear chain structure becomes favorable due to the intra-chain interactions, that make it 213 meV per molecule more favorable than the corresponding RCP structure in the $\left(8 \times 4\sqrt{3}\right)$-rect supercell (Fig. 6(c)). If the molecular density is increased by decreasing the chain-chain distance such that the chain model resides in the $\left(7 \times 4\sqrt{3}\right)$-rect slab, the Co-DPP at the neighboring chain needs to move a copper lattice (2.55 Å) closer in order to adsorb at its preferred bridge site, which results in a very short chain-chain distance (~11 Å), falling into the repulsive interaction range (Fig. 5(c)). In contrast, in the RCP structural model (Fig.6(b)), as L- and R-Co-DPP adsorb at different adsorption sites, the molecule-molecule distance between L- and R-Co-DPP can be reduced to 12.7 Å, the molecular density increases to 0.63 molecules / nm^2, at which

the RCP structure profits from intermolecular interactions in line with the condition of the formation of the RCP structure in the gas phase calculations. The RCP structure in the $(7 \times 4\sqrt{3})$-rect supercell has a 175 meV per molecule lower adsorption energy than the chain model in the same cell (Fig.6(d)). Therefore, the phase transition from linear chain structure to RCP structure is a natural choice of the system at slightly lower molecular coverage than in the gas-phase model if the substrate is accounted for.

We find that the phase transition of Co-DPP from an enantiopure linear chain structure to a racemic close-packed structure follows Wallach's rule[57,58], which states that the density of a racemic crystal is higher than that of enantiopure samples. This behavior can be understood by looking at the adsorption energy (including intermolecular interactions). The phase transition of Co-DPP is due to the subtle interplay (competition) between the molecule-substrate and the molecule-molecule interactions. However, the templating effect of the substrate becomes less important when the molecular density reaches $0.7\,\text{molecules}/\text{nm}^2$ (corresponding to ~1 monolayer coverage). At such high density, Co-DPP forms a most densely packed brick-layer structure, in which the chiral nature of the molecules can no longer be sensed. Hence, the adsorption geometry of Co-DPP may also change at that molecular density.[59]

CONCLUSIONS

In summary, we experimentally observed a phase transition of the self-assembly of Co-DPP on Cu(111) from a chiral enantiopure linear chain structure to a racemic close packed structure as a function of molecular coverage. We analyzed the system using DFT calculations showing that the phase change is due to the interplay between molecule-substrate and molecule-molecule interactions, the latter ones becoming the main driving force when the molecular density is at full coverage. This system is a typical example that follows the Wallach's rule, our studies will help to

understand the thermodynamic process and self-assembly behaviors of organic molecules on surfaces, paving the ways to further reveal the coverage dependent performance of organic layer devices.

AUTHOR INFORMATION

Corresponding Author

*Feifei Xiang: feifei.xiang@empa.ch

*M. Alexander Schneider: alexander.schneider@fau.de

Present Addresses

† nanotech@surfaces Laboratory, Empa, Swiss Federal Laboratories for Materials Science & Technology, Überlandstrasse 129 8600 Dübendorf, Switzerland

Notes

The authors declare no competing financial interest.

ACKNOWLEDGMENT

F.X. and M.A.S. acknowledge support from the Deutsche Forschungsgemeinschaft through the research unit FOR1878/funCOS+ RRZE for computing time.

REFERENCES

(1) Usov, I.; Nyström, G.; Adamcik, J.; Handschin, S.; Schütz, C.; Fall, A.; Bergström, L.; Mezzenga, R. Understanding Nanocellulose Chirality and Structure-Properties Relationship at the Single Fibril Level. *Nat. Commun.* **2015**, *6*, 1–11.

(2) Inaki, M.; Liu, J.; Matsuno, K. Cell Chirality: Its Origin and Roles in Left-Right Asymmetric Development. *Philos. Trans. R. Soc. B Biol. Sci.* **2016**, *371*, 1–9.

(3) Blackmond, D. G. The Origin of Biological Homochirality. *Philos. Trans. R. Soc. B Biol. Sci.* **2011**, *366*, 2878–2884.

(4) Hein, J. E.; Blackmond, D. G. On the Origin of Single Chirality of Amino Acids and Sugars in Biogenesis. *Acc. Chem. Res.* **2012**, *45*, 2045–2054.

(5) Reetz, M. T. Controlling the Enantioselectivity of Enzymes by Directed Evolution: Practical and Theoretical Ramifications. *Proc. Natl. Acad. Sci.* **2004**, *101*, 5716–5722.

(6) Roger J. Crossley. *Chirality and Biological Activity of Drugs*; CRC Press, 1995.

(7) Ernst, K. H. Molecular Chirality at Surfaces. In *Surface and Interface Science*; John Wiley & Sons, Ltd, 2016; Vol. 6, pp 695–748.

(8) Seibel, J.; Parschau, M.; Ernst, K. H. From Homochiral Clusters to Racemate Crystals: Viable Nuclei in 2D Chiral Crystallization. *J. Am. Chem. Soc.* **2015**, *137*, 7970–7973.

(9) Barlow, S. M.; Louafi, S.; Le Roux, D.; Williams, J.; Muryn, C.; Haq, S.; Raval, R. Polymorphism in Supramolecular Chiral Structures of R- and S-Alanine on Cu(1 1 0). *Surf. Sci.* **2005**, *590*, 243–263.

(10) Wang, X. Y.; Urgel, J. I.; Barin, G. B.; Eimre, K.; Di Giovannantonio, M.; Milani, A.; Tommasini, M.; Pignedoli, C. A.; Ruffieux, P.; Feng, X.; Fasel, R.; Müllen, K.; Narita, A. Bottom-Up Synthesis of Heteroatom-Doped Chiral Graphene Nanoribbons. *J. Am. Chem. Soc.* **2018**, *140*, 9104–9107.

(11) Merino-Díez, N.; Li, J.; Garcia-Lekue, A.; Vasseur, G.; Vilas-Varela, M.; Carbonell-Sanromà, E.; Corso, M.; Ortega, J. E.; Peña, D.; Pascual, J. I.; De Oteyza, D. G. Unraveling

the Electronic Structure of Narrow Atomically Precise Chiral Graphene Nanoribbons. *J. Phys. Chem. Lett.* **2018**, *9*, 25–30.

(12) Xiang, F.; Lu, Y.; Wang, Z.; Ju, H.; Di Filippo, G.; Li, C.; Liu, X.; Leng, X.; Zhu, J.; Wang, L.; Schneider, M. A. On-Surface Synthesis of Chiral π-Conjugate Porphyrin Tapes by Substrate-Regulated Dehydrogenative Coupling. *J. Phys. Chem. C* **2019**, *123*, 23007–23013.

(13) Ernst, K. H. On the Validity of Calling Wallach's Rule Wallach's Rule. *Isr. J. Chem.* **2017**, *57*, 24–30.

(14) Dutta, S.; Gellman, A. J. Enantiomer Surface Chemistry: Conglomerate versus Racemate Formation on Surfaces. *Chem. Soc. Rev.* **2017**, *46*, 7787–7839.

(15) Yu, M. N.; Li, Y. X.; Xu, M.; Lin, J. Y.; Gu, J. Bin; Sun, N.; Lin, D. Q.; Wang, Y. X.; Xie, L. H.; Huang, W. Molecular Conformational Transition of Chiral Conjugated Enantiomers Dominated by Wallach's Rule. *J. Mater. Chem. C* **2021**, *9*, 6991–6995.

(16) Friščić, T.; Fábián, L.; Burley, J. C.; Reid, D. G.; Duer, M. J.; Jones, W. Exploring the Relationship between Cocrystal Stability and Symmetry: Is Wallach's Rule Applicable to Multi-Component Solids? *Chem. Commun.* **2008**, *0*, 1644–1646.

(17) Otero-De-La-Roza, A.; Hein, J. E.; Johnson, E. R. Reevaluating the Stability and Prevalence of Conglomerates: Implications for Preferential Crystallization. *Cryst. Growth Des.* **2016**, *16*, 6055–6059.

(18) Dunitz, J. D.; Gavezzotti, A. Proteogenic Amino Acids: Chiral and Racemic Crystal

Packings and Stabilities. *J. Phys. Chem. B* **2012**, *116*, 6740–6750.

(19) Kostyanovsky, R. G.; Lakhvich, F. A.; Philipchenko, P. M.; Lenev, D. A.; Torbeev, V. Y.; Lyssenko, K. A. (±)-Trans-1,2-Diaminocyclohexane Crystallises as a Conglomerate. *Mendeleev Commun.* **2002**, *12*, 147–148.

(20) Irziqat, B.; Berger, J.; Mendieta-Moreno, J. I.; Sundar, M. S.; Bedekar, A. V.; Ernst, K. H. Transition from Homochiral Clusters to Racemate Monolayers during 2D Crystallization of Trioxa[11]Helicene on Ag(100). *ChemPhysChem* **2021**, *22*, 293–297.

(21) Nguyen, T. N. H.; Xue, S.; Tegenkamp, C. Heterochiral Dimer Formation of α-l- A Nd α-d-Polyalanine Molecules on Surfaces. *J. Phys. Chem. C* **2020**, *124*, 11075–11080.

(22) Xu, L.; Miao, X.; Cui, L.; Liu, P.; Miao, K.; Chen, X.; Deng, W. Chiral Transition of the Supramolecular Assembly by Concentration Modulation at the Liquid/Solid Interface. *J. Phys. Chem. C* **2015**, *119*, 17920–17929.

(23) Schiffrin, A.; Reichert, J.; Pennec, Y.; Auwarter, W.; Alexander Weber-Bargioni; Marschall, M.; Angela, M. D.; Cvetko, D.; Bavdek, G.; Cossaro, A.; Morgante, A.; Barth, J. V. Self-Assembly of l-Methionine on Cu(111): Steering Chiral Organization by Substrate Reactivity and Thermal Activation. *J. Phys. Chem. C* **2009**, *113*, 12101–12108.

(24) Mugarza, A.; Lorente, N.; Ordejón, P.; Krull, C.; Stepanow, S.; Bocquet, M. L.; Fraxedas, J.; Ceballos, G.; Gambardella, P. Orbital Specific Chirality and Homochiral Self-Assembly of Achiral Molecules Induced by Charge Transfer and Spontaneous Symmetry Breaking. *Phys. Rev. Lett.* **2010**, *105*, 30–33.

(25) Song, H.; Zhu, H.; Huang, Z.; Zhang, Y.; Zhao, W.; Liu, J.; Chen, Q.; Yin, C.; Xing, L.; Peng, Z.; Liao, P.; Wang, Y.; Wang, Y.; Wu, K. Steering the Achiral into Chiral with a Self-Assembly Strategy. *ACS Nano* **2019**, *13*, 7202–7208.

(26) Gesquière, A.; Jonkheijm, P.; Hoeben, F. J. M.; Schenning, A. P. H. J.; De Feyter, S.; De Schryver, F. C.; Meijer, E. W. 2D-Structures of Quadruple Hydrogen Bonded Oligo(p-Phenylenevinylene)s on Graphite: Self-Assembly Behavior and Expression of Chirality. *Nano Lett.* **2004**, *4*, 1175–1179.

(27) Xiao, W.; Feng, X.; Ruffieux, P.; Gröning, O.; Müllen, K.; Fasel, R. Self-Assembly of Chiral Molecular Honeycomb Networks on Au(111). *J. Am. Chem. Soc.* **2008**, *130*, 8910–8912.

(28) Li, C.; Li, R.; Xu, Z.; Li, J.; Zhang, X.; Li, N.; Zhang, Y.; Shen, Z.; Tang, H.; Wang, Y. Packing Biomolecules into Sierpiński Triangles with Global Organizational Chirality. *J. Am. Chem. Soc.* **2021**, *143*, 14417–14421.

(29) Écija, D.; Seufert, K.; Heim, D.; Auwärter, W.; Aurisicchio, C.; Fabbro, C.; Bonifazi, D.; Barth, J. V. Hierarchic Self-Assembly of Nanoporous Chiral Networks with Conformationally Flexible Porphyrins. *ACS Nano* **2010**, *4*, 4936–4942.

(30) Blüm, M.-C.; Ćavar, E.; Pivetta, M.; Patthey, F.; Schneider, W.-D. Conservation of Chirality in a Hierarchical Supramolecular Self-Assembled Structure with Pentagonal Symmetry. *Angew. Chemie* **2005**, *117*, 5468–5471.

(31) Tsuboi, T.; Wasai, Y.; Nabatova-Gabain, N. Optical Constants of Platinum Octaethyl Porphyrin in Single-Layer Organic Light Emitting Diode Studied by Spectroscopic

Ellipsometry. *Thin Solid Films* **2006**, *496*, 674–678.

(32) Kurlekar, K.; Anjali, A.; Sonalin, S.; Imran, P. M.; Nagarajan, S. Solution-Processable Meso-Triarylamine Functionalized Porphyrins with a High Mobility and ON/OFF Ratio in Bottom-Gated Organic Field-Effect Transistors. *ACS Appl. Electron. Mater.* **2020**, *2*, 3402–3408.

(33) Zampetti, A.; Minotto, A.; Cacialli, F. Near-Infrared (NIR) Organic Light-Emitting Diodes (OLEDs): Challenges and Opportunities. *Adv. Funct. Mater.* **2019**, *29*, 1807623.

(34) Verykios, A.; Papadakis, M.; Soultati, A.; Skoulikidou, M. C.; Papaioannou, G.; Gardelis, S.; Petsalakis, I. D.; Theodorakopoulos, G.; Petropoulos, V.; Palilis, L. C.; Fakis, M.; Vainos, N. A.; Alexandropoulos, D.; Davazoglou, D.; Pistolis, G.; Argitis, P.; Coutsolelos, A. G.; Vasilopoulou, M. Functionalized Zinc Porphyrins with Various Peripheral Groups for Interfacial Electron Injection Barrier Control in Organic Light Emitting Diodes. *ACS Omega* **2018**, *3*, 10008–10018.

(35) Winkelmann, C. B.; Ionica, I.; Chevalier, X.; Royal, G.; Bucher, C.; Bouchiat, V. Optical Switching of Porphyrin-Coated Silicon Nanowire Field Effect Transistors. *Nano Lett.* **2007**, *7*, 1454–1458.

(36) Flores-Sánchez, R.; Gámez, F.; Lopes-Costa, T.; Pedrosa, J. M. A Calixarene Promotes Disaggregation and Sensing Performance of Carboxyphenyl Porphyrin Films. *ACS Omega* **2020**, *5*, 6299–6308.

(37) Xiang, F.; Gemeinhardt, A.; Schneider, M. A. Competition between Dehydrogenative Organometallic Bonding and Covalent Coupling of an Unfunctionalized Porphyrin on

Cu(111). *ACS Nano* **2018**, *12*, 1203–1210.

(38) Xiang, F.; Li, C.; Wang, Z.; Liu, X.; Jiang, D.; Leng, X.; Ling, J.; Wang, L. Direct Observation of Copper-Induced Metalation of 5,15-Diphenylporphyrin on Au(111) by Scanning Tunneling Microscopy. *Surf. Sci.* **2015**, *633*, 46–52.

(39) Lepper, M.; Schmitt, T.; Gurrath, M.; Raschmann, M.; Zhang, L.; Stark, M.; Hölzel, H.; Jux, N.; Meyer, B.; Schneider, M. A.; Steinrück, H. P.; Marbach, H. Adsorption Behavior of a Cyano-Functionalized Porphyrin on Cu(111) and Ag(111): From Molecular Wires to Ordered Supramolecular Two-Dimensional Aggregates. *J. Phys. Chem. C* **2017**, *121*, 26361–26371.

(40) Moreno-López, J. C.; Mowbray, D. J.; Pérez Paz, A.; De Campos Ferreira, R. C.; Ceccatto Dos Santos, A.; Ayala, P.; De Siervo, A. Roles of Precursor Conformation and Adatoms in Ullmann Coupling: An Inverted Porphyrin on Cu(111). *Chem. Mater.* **2019**, *31*, 3009–3017.

(41) Ditze, S.; Stark, M.; Drost, M.; Buchner, F.; Steinrück, H.-P.; Marbach, H. Activation Energy for the Self-Metalation Reaction of 2H-Tetraphenylporphyrin on Cu(111). *Angew. Chem. Int. Ed.* **2012**, *51*, 10898–10901.

(42) Horcas, I.; Fernández, R.; Gómez-Rodríguez, J. M.; Colchero, J.; Gómez-Herrero, J.; Baro, A. M. WSXM : A Software for Scanning Probe Microscopy and a Tool for Nanotechnology. *Rev. Sci. Instrum.* **2007**, *78*, 013705.

(43) Kresse, G.; Furthmüller, J. Efficient Iterative Schemes for *Ab Initio* Total-Energy Calculations Using a Plane-Wave Basis Set. *Phys. Rev. B* **1996**, *54*, 11169–11186.

(44) Kresse, G.; Furthmüller, J. Efficiency of Ab-Initio Total Energy Calculations for Metals and Semiconductors Using a Plane-Wave Basis Set. *Comput. Mater. Sci.* **1996**, *6*, 15–50.

(45) Kresse, G.; Joubert, D. From Ultrasoft Pseudopotentials to the Projector Augmented-Wave Method. *Phys. Rev. B* **1999**, *59*, 1758–1775.

(46) Perdew, J. P.; Burke, K.; Ernzerhof, M. Generalized Gradient Approximation Made Simple. *Phys. Rev. Lett.* **1996**, *77*, 3865–3868.

(47) Klime, J.; Bowler, D. R.; Michaelides, A. Van Der Waals Density Functionals Applied to Solids. *Phys. Rev. B - Condens. Matter Mater. Phys.* **2011**, *83*, 195131.

(48) Tersoff, J.; Hamann, D. R. Theory of the Scanning Tunneling Microscope. *Phys. Rev. B* **1985**, *31*, 805–813.

(49) Fan, Q.; Wang, T.; Dai, J.; Kuttner, J.; Hilt, G.; Gottfried, J. M.; Zhu, J. On-Surface Pseudo-High-Dilution Synthesis of Macrocycles: Principle and Mechanism. *ACS Nano* **2017**, *11*, 5070–5079.

(50) Rossa, L.; Vögtle, F. Synthesis of Medio- and Macrocyclic Compounds by High Dilution Principle Techniques; Springer, Berlin, Heidelberg, 2012; pp 1–86.

(51) Xiang, F.; Schmitt, T.; Raschmann, M.; Schneider, M. A. Adsorption and Self-Assembly of Porphyrins on Ultrathin CoO Films on Ir(100). *Beilstein J. Nanotechnol.* **2020**, *11*, 1516–1524.

(52) Voigt, J.; Roy, M.; Baljozović, M.; Wäckerlin, C.; Coquerel, Y.; Gingras, M.; Ernst, K. H. Unbalanced 2D Chiral Crystallization of Pentahelicene Propellers and Their Planarization

into Nanographenes. *Chem. - A Eur. J.* **2021**, *27*, 10251–10254.

(53) Martinez, C. R.; Iverson, B. L. Rethinking the Term “Pi-Stacking.” *Chem. Sci.* **2012**, *3*, 2191.

(54) Hunter, C. A. Meldola Lecture. The Role of Aromatic Interactions in Molecular Recognition. *Chem. Soc. Rev.* **1994**, *23*, 101–109.

(55) Andersson, Y.; Hult, E.; Rydberg, H.; Apell, P.; Lundqvist, B. I.; Langreth, D. C. Van Der Waals Interactions in Density Functional Theory. In *Electronic Density Functional Theory*; Springer US: Boston, MA, 1998; pp 243–260.

(56) Hermann, J.; DiStasio, R. A.; Tkatchenko, A. First-Principles Models for van Der Waals Interactions in Molecules and Materials: Concepts, Theory, and Applications. *Chem. Rev.* **2017**, *117*, 4714–4758.

(57) Wallach, O. Zur Kenntniss Der Terpene Und Der Ätherischen Oele. *Justus Liebigs Ann. Chem.* **1895**, *286*, 90–118.

(58) Brock, C. P.; Schweizer, W. B.; Dunitz, J. D. On the Validity of Wallach’s Rule: On the Density and Stability of Racemic Crystals Compared with Their Chiral Counterparts. *J. Am. Chem. Soc.* **1991**, *113*, 9811–9820.

(59) Papageorgiou, A. C.; Knecht, P.; Ryan, P. T. P.; Duncan, D. A.; Jiang, L.; Reichert, J.; Deimel, P. S.; Haag, F.; Küchle, J. T.; Allegretti, F.; Lee, T. L.; Schwarz, M.; Garnica, M.; Auwärter, W.; Seitsonen, A. P.; Barth, J. V. Tunable Interface of Ruthenium Porphyrins and Silver. *J. Phys. Chem. C* **2021**, *125*, 3215–3224.

TOC image

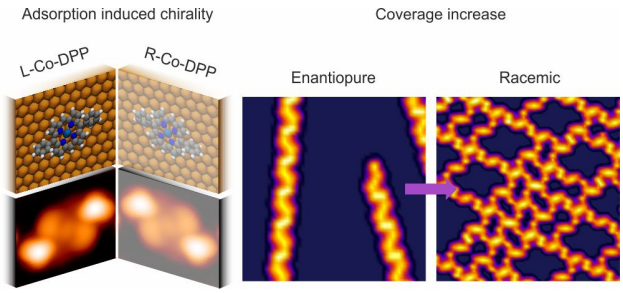
Adsorption induced chirality
Coverage increase
L-Co-DPP
R-Co-DPP
Enantiopure
Racemic